

Supporting Information:

Macroscopic Salt Rejection through Electrostatically Gated Nanoporous Graphene

Roman M. Wyss,^{†,||} Tian Tian,^{‡,||} Khadija Yazda,[¶] Hyung Gyu Park,^{*,¶,§} and
Chih-Jen Shih^{*,‡}

[†]*Soft Materials, Department of Materials, Eidgenössische Technische Hochschule (ETH) Zürich,
Vladimir-Prelog-Weg 1-5, Zürich CH-8093, Switzerland.*

[‡]*Institute for Chemical and Bioengineering Department of Chemistry and Applied Biosciences,
Eidgenössische Technische Hochschule (ETH) Zürich, Vladimir-Prelog-Weg 1-5, Zürich
CH-8093, Switzerland.*

[¶]*Nanoscience for Energy Technology and Sustainability, Department of Mechanical and Process
Engineering, Eidgenössische Technische Hochschule (ETH) Zürich, Tannenstrasse 3, Zürich
CH-8092, Switzerland.*

[§]*Mechanical Engineering, Pohang University of Science and Technology (POSTECH), 77
Cheongam-ro, Nam-gu, Pohang, Gyeongbuk, 37673, Republic of Korea.*

^{||}*R. M. W. and T. T. contributed equally to this work*

E-mail: iduserpark@gmail.com; chih-jen.shih@chem.ethz.ch

S1 Graphene membrane manufacturing and results.

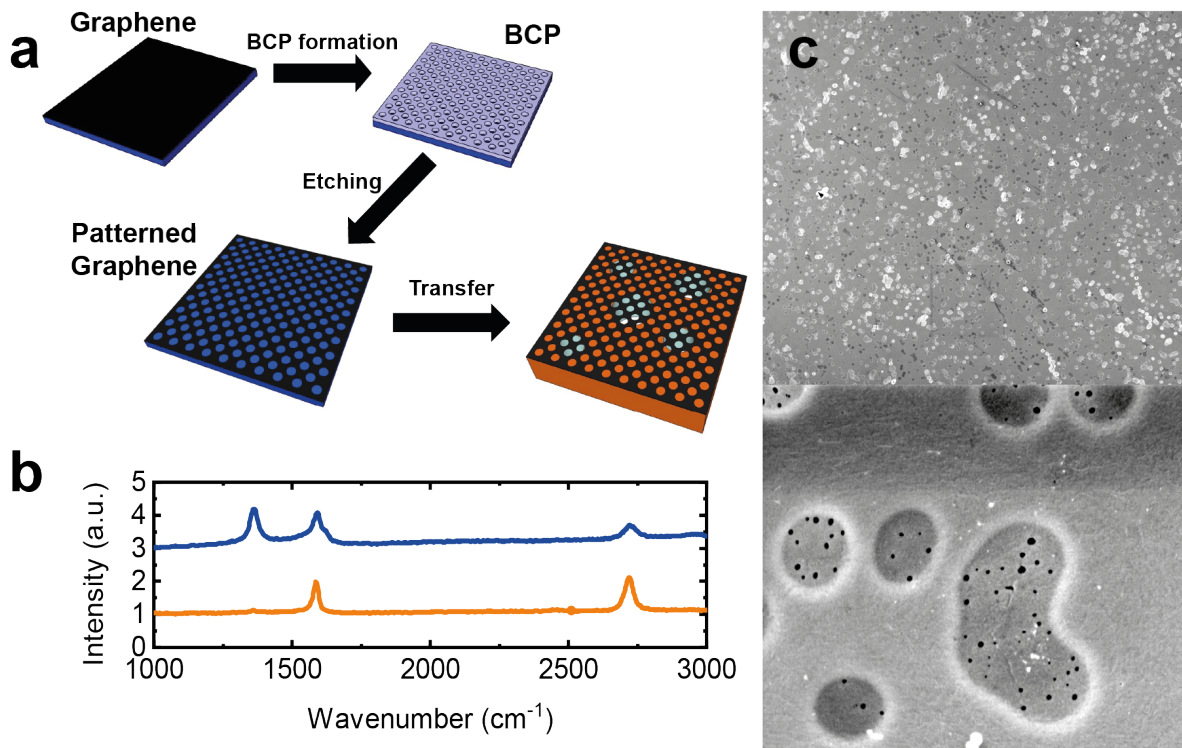


Figure S1: **a.** Schematic of manufacturing process for patterning of double layer graphene. Graphene is synthesized and transferred to a substrate (glass slide) to yield a double layer. s-BCP is spin-coated and annealed in vacuum to undergo microphase separation, followed by plasma etch and wet etching yielding a porous polystyrene (PS) mask. Anisotropic etching of the mask leads to patterning the underlying graphene, PS is removed by thermal annealing. The porous graphene is then transferred to a substrate (e.g. PCTE). **b.** Raman spectra of graphene before (orange curve) and after (blue curve) patterning. An increase of the D-peak at 1350 cm^{-1} indicates the formation of defects and edges. The spectra have been normalized to the G-peak intensity and offset for better comparison. **c.** SEM graph of patterned graphene on PCTE at lower (top) and higher (bottom) magnifications.

S2 Ion diffusion measurement and calculation

The ion diffusion through b-PCTE has been performed using a sample sandwiched between two layers of Aluminum tape where the edges have been sealed using water-resistant epoxy (ACS Marine Epoxy) to avoid interlayer leakage pathways.^{S1} The sample was inserted in the fixture

following the same wetting procedure described in the main text Methods and was kept wet for the entire series of experiments.

Table S1: Different diffusivity values for the anions and cations of the salts used in this work.^{S2} The theoretical diffusion through PCTE can be calculated using Eq. 1 in the main text and the diffusivities of the respective anion and cation.

Salt	D ($10^{-9} \text{ m}^2 \cdot \text{s}^{-1}$)
K^+	1.95
Na^+	1.33
Li^+	1.03
SO_4^{2-}	1.06
Ca^{2+}	0.79
Mg^{2+}	0.7
$\text{Fe}[(\text{CN})_6]^{3-}$	0.90
Cl^-	2.03

The conductivity increase s ($\text{mS} \cdot \text{cm}^{-1} \cdot \text{d}^{-1}$) is converted into ion permeation rates J_{PCTE} ($\text{mol} \cdot \text{m}^{-2} \cdot \text{s}^{-1}$) by use of a calibration factor c_f , the volume of LCR (V_{LCR}), the area of the membrane A and the time t as:

$$J_{\text{PCTE}} = \frac{sV_{\text{LCR}}}{c_f A t} \quad (\text{S1})$$

The calibration factors for all salts have been obtained by a linear fit of conductivity *versus* concentration for 4 solutions with concentrations from 10^{-4} M to 10^{-2} M and extracting the resulting slope. The rest of the factors are $V_{\text{LCR}} = 7.33 \text{ mL}$, $A = 9 \times 10^{-6} \text{ m}^2$. Table S2 shows the averaged conductivity increase s , the extracted calibration factors c_f and the resulting ion permeation rates using Eq. S1. The values from this table are shown in main text Fig.2b (blue bars).

Table S2: Extracted slope s as an averaged result from 3 consecutive measurements, the calibration factors c_f and the resulting ion permeation J_{PCTE} through b-PCTE membranes for all salts.

Salt	s ($\text{mS} \cdot \text{cm}^{-1} \cdot \text{d}^{-1}$)	c_f ($\text{mS} \cdot \text{cm}^{-1} \cdot \text{mol}^{-1} \cdot \text{L}$)	J_{PCTE} ($10^6 \text{ mol} \cdot \text{m}^{-2} \cdot \text{s}^{-1}$)
KCl	$1.51 \pm 0.27 \times 10^{-2}$	106	1.34 ± 0.24
NaCl	$9.90 \pm 0.17 \times 10^{-3}$	91	1.02 ± 0.02
LiCl	$6.03 \pm 0.80 \times 10^{-3}$	83	0.682 ± 0.090
CaCl_2	$1.25 \pm 0.1 \times 10^{-2}$	149	0.789 ± 0.063
MgSO_4	$8.80 \pm 1.2 \times 10^{-3}$	130	0.633 ± 0.084
$\text{K}_3[\text{Fe}(\text{CN})_6]$	$2.40 \pm 0.28 \times 10^{-2}$	395	0.575 ± 0.063
K_2SO_4	$1.98 \pm 0.20 \times 10^{-2}$	258	0.722 ± 0.073

The experimentally observed flux reduction through PG-PCTE upon gating, η , for all the salts studied here (with concentration of 0.1 mM in HCR), can be found in Fig. S2. The effective salt rejection ratio ξ is then extracted using main text Eq. 3.

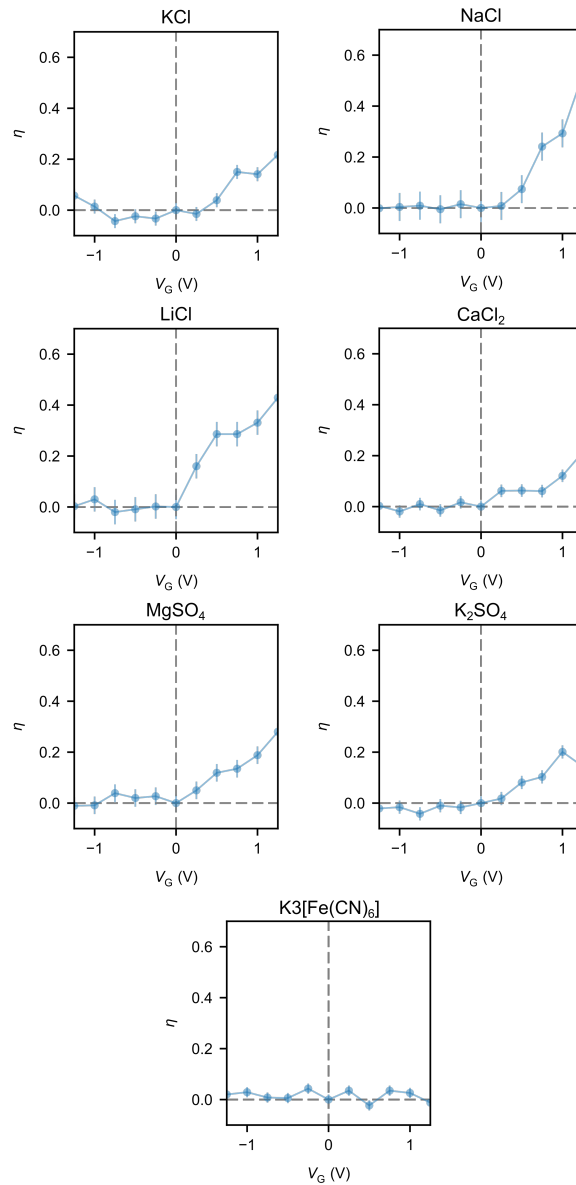


Figure S2: Measured η values as function of V_G for various salts used in this work. The concentration in HCR is 0.1 mM in all cases.

S3 Control experiment with copper tape

We make sure that the applied voltage is effectively applied via the graphene membrane and not through leakage directly coupling the copper tape to the ionic solution. For this purpose, we use a device as in Fig.1a, omitting the graphene and measuring the current through the membrane with the Autolab electrochemical workstation using the membrane as working electrode and a platinum wire as counter/reference electrode 3.5 cm apart in 0.1 mM KCl. When no graphene is inserted in the device, a current in the baseline range (~ 0.1 nA) is observed, indicating no current passing from the membrane. However, if graphene is inserted, a current in the range of ~ 10 - 100 nA is measured. If the copper tape is in contact with the solution when omitting the Kapton tape, the current increases to ~ 1 - 10 μ A, independent of the exposed area of the copper tape to the solution.

S4 Circuit analog model of transport through PG-PCTE

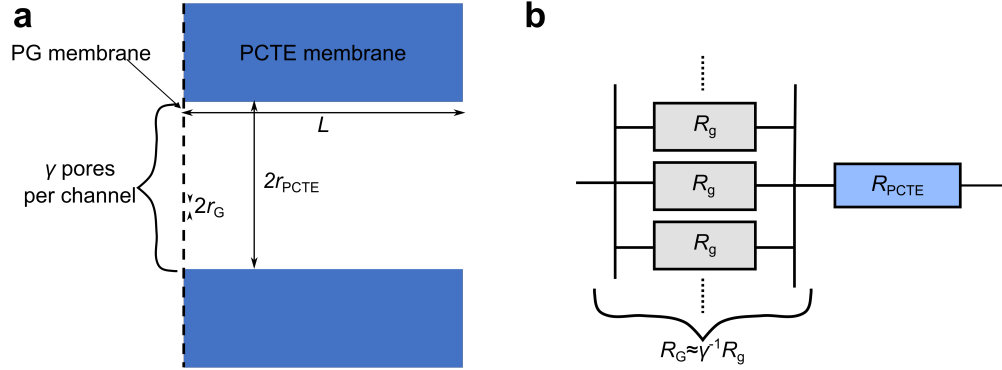


Figure S3: Simple circuit analog model for the transport through PG-PCTE membrane. **a.** Schematic of PG-PCTE membrane in cross-section view. **b.** Model for transport resistance in analogy to an electric circuit. This schematic depicts a cut through a PG-PCTE membrane showing a single PCTE pore and multiple graphene pores.

The ionic transport through the PG-PCTE membrane is the concerted effect the transport resistance through PG and PCTE membranes, respectively. As schematically shown in Fig. S3, the overall transport resistance of the system is composed of the series resistance R_{G} and R_{PCTE} , respectively. For both PG and PCTE membranes, the resistance R is defined as the ratio between the

concentration between HCR and LCR Δc , and the total diffusive current I as:

$$R_i = \left| \frac{\Delta c}{I_i} \right| = \left| \frac{\Delta c}{J_i A_i} \right| \quad (\text{S2})$$

where i denotes the membrane type and A_i is the area of the pore. We further treat R_G as the effective resistance of γ parallel resistors with individual resistance R_g , where γ is the average number of PG pores per PCTE channel, and R_g is the average transport resistance per PG pore. The value of γ is determined from geometric analysis of both membranes: given the pore number density of PG ($\sim 1.25 \times 10^{14} \text{ m}^{-2}$), the pore number density of PCTE ($\sim 1.50 \times 10^{12} \text{ m}^{-2}$), and the percentage of PCTE pores with PG on top (~ 0.13), γ is determined to be ~ 10.83 .

The objective of the circuit analog model is to find effective salt rejection ratio through PG, ξ extracted from the experimental η values (defined in main text Eq. 2). By defining $R_G^0 = R_G(V_G = 0)$, $\delta = R_{\text{PCTE}}/R_G^0$, $\chi = R_G/R_G^0$, η is rewritten using transport resistances as:

$$\begin{aligned} \eta &= 1 - \frac{(R_{\text{PCTE}} + R_G)^{-1}}{(R_{\text{PCTE}} + R_G^0)^{-1}} \\ &= 1 - \frac{\delta + 1}{\delta + R_G/R_G^0} \\ &= 1 - \frac{\delta + 1}{\delta + \chi} \end{aligned} \quad (\text{S3})$$

Consequently, the salt rejection ratio ξ , is associated with χ by $\xi = 1 - \chi^{-1}$ and is related with δ and η via:

$$\begin{aligned} \xi &= 1 - \chi^{-1} \\ &= \frac{(\delta + 1)\eta}{\delta\eta + 1} \end{aligned} \quad (\text{S4})$$

which is main text Eq. 3. When $0 < \eta < 1$ (salt rejection regime) and $\delta > 0$, Eq. S4 always guarantees $\xi > \eta$, since $\delta + 1$ is always larger than $\delta\eta + 1$. In other words, due to the existence of R_{PCTE} , the effective salt rejection through PG upon gating is always larger than that experimentally observed.

Next we seek the value of δ , the resistance ratio between the PCTE and PG membranes, without

gating. The range of δ can be estimated from experimental data in main text Fig. 2b using the relation:

$$\delta = \left(\frac{J_{\text{PCTE}}}{J_{\text{PG}}^0} - 1 \right)^{-1} \quad (\text{S5})$$

by assuming the validity of the circuit analog model for all salt systems. As shown in Fig. S4, the experimentally estimated value of δ varies from 1 to 5, indicating that the resistance of the PG membrane is dominating in the PG-PCTE system. δ can also be estimated using geometric

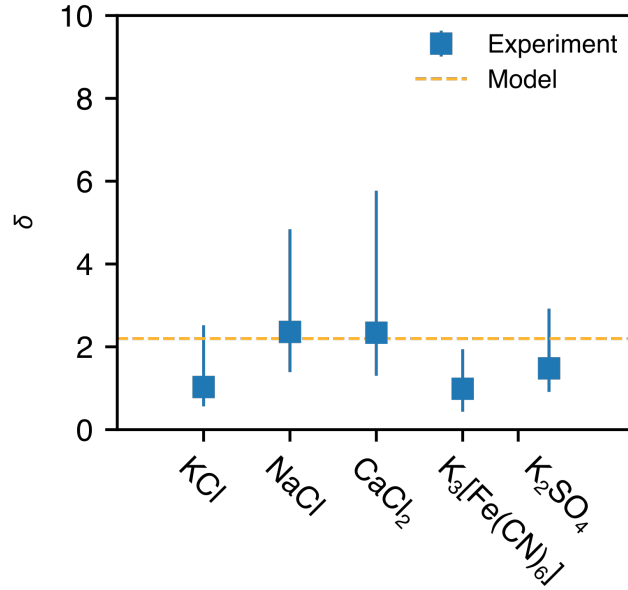


Figure S4: Comparison between the δ value estimated from simple geometric model (Eq. S7) and from experimental value (Eq. S5), showing good agreement between the two methods.

parameters of both membranes. For a long PCTE channel with length L and r_{PCTE} , R_{PCTE} has power law of L/r_{PCTE}^2 , while for a graphene pore with radius r_{G} and vanishing thickness, the resistance of individual pore R_{g}^0 has power law $1/r_{\text{G}}$,^{S3} which are expressed as:

$$R_{\text{PCTE}} = k_{\text{PCTE}} \frac{L}{r_{\text{PCTE}}^2} \quad (\text{S6a})$$

$$R_{\text{g}}^0 = k_{\text{g}} \frac{1}{r_{\text{G}}} \quad (\text{S6b})$$

where k_{PCTE} and k_{g} are the coefficient associated with PCTE and PG membranes, respectively.

The value of δ is then expressed as:

$$\delta = \frac{R_{\text{PCTE}}}{R_{\text{G}}^0} = \frac{k_{\text{PCTE}}}{k_{\text{g}}} \frac{L r_{\text{G}} \gamma}{r_{\text{PCTE}}^2} \quad (\text{S7})$$

Here we take $L=24 \mu\text{m}$, $r_{\text{G}}=10 \text{ nm}$, $r_{\text{PCTE}}=200 \text{ nm}$. From simple Fick's law, the coefficient k_{PCTE} is determined as $1/(D_{\pm}\pi)$. On the other hand k_{G} varies by the choice of model, ranging from $3\pi/D_{\pm}$ using the analog of the Sampson formula for fluid,^{S4,S5} to $1/(2D_{\pm})$ from the Hill formula for disk absorption model.^{S6,S7} As a result the theoretical value of δ has lower bound of ~ 2.2 (Sampson formula, orange line in Fig. S4) to ~ 40.5 (Hill formula). We note our experimental values of δ is in good agreement estimated from the Sampson formula (which we use in the main text) while lower than the Hill formula. Having a higher estimated value of δ could yield unreasonably high value of ξ and the influence of concentration is deviated from our theoretical predictions. Further theoretical analysis taking nonidealities including surface adsorption and chemical nature of pore edge, is required to have better understanding of graphene's transport resistance.

S5 KCl Debye length and conductivity

Table S3 gives an overview about the measured conductivities and their calculated Debye length values for KCl. The information is used to plot the ξ versus c_0 curve.

Table S3: Conductivity and calculated Debye lengths of various KCl concentrations in order to obtain rejection versus concentration curves.

c_0 (mM)	Conductivity ($\text{mS}\cdot\text{cm}^{-1}$)	λ_{D} (nm)
0.1	1.90×10^{-2}	30.4
0.33	5.41×10^{-2}	16.0
1	1.33×10^{-1}	10.0
3.3	5.13×10^{-1}	6.0
10	1.08	3.3

S6 Measurement of charge carrier density of patterned graphene

The intrinsic charge carrier density of graphene was measured using a field electron transistor (FET) in air with a 300nm SiO₂ as a gate. The device setup is shown in Fig. S5a, where the source and drain electrodes were deposited onto the PG sample transferred onto 300nm SiO₂ on doped Silicon. The characteristic drain-source current I_{DS} as a function of V_G is shown in Fig. S5. The charge-neutral point gate voltage V_{CNP} is measured to be 2.8 V. Using the capacitance of the SiO₂ dielectric, we an intrinsic charge density of $\sim 1.4 \times 10^{11} e \cdot \text{cm}^{-2}$, and a shift in the PG's Fermi level by ~ 48 meV, which is negligible compared with the gate-induced charge density in our experiments. Therefore, the assumption that the PG sample is intrinsic without gating, is justified.

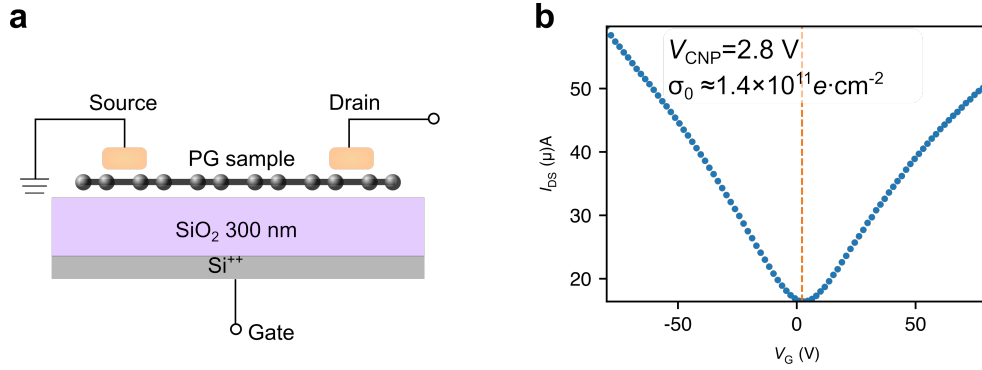


Figure S5: Characterization of the intrinsic charge density of the PG sample using field effect transistor. **a.** The setup of the PG-FET. **b.** The I_{DS} as a function of V_G . The charge neutral point gate voltage is determined as ~ 2.8 V, corresponding to an intrinsic charge density of $\sim 1.4 \times 10^{11} e \cdot \text{cm}^{-2}$, which is negligible compared with the gate-induced charges.

S7 Further discussion about the ionic pathway near the graphene pore

In this section we provide a more detailed discussion about the different ionic pathways through the graphene nanopore upon gating in main text Fig. 4b. As discussed in the main text, the ionic migration arises from both diffusion (caused by concentration gradient) and electrostatic drift (caused by electric field). The effect of salt rejection can be viewed as follows: when $V_G = 0$, the flux J_G is solely contributed by the concentration gradient, while after applying a positive V_G , distinct pathways for cations / anions are created and the drift flux counteracts the diffusion.

Applying a positive V_G changes the surface distribution of the cations / anions. To see this, we plot the concentrations of cations (c_+) and anions (c_-) near a graphene nanopore with $r_G = 10$ nm, $c_0 = 0.1$ mM and $V_G = 0.75$ V, as shown in Fig. S6a and S6b, respectively. The cations are depleted from the graphene surface, while the anions are accumulated due to positive ψ_G . The anion concentration at the graphene surface is enhanced ~ 35 times compared with the bulk concentration in HCR. The thickness of the depletion / accumulation layer is affected by the bulk concentration. Here we show this by comparing the radial distribution of c_+ and c_- along the $z = 0$ line within the graphene pore. Fig. S7 shows such radial ionic concentration distribution at different c_0 and V_G levels. When $c_0 = 0.1$ mM, λ_D is larger than r_G , and the external gate voltage V_G has control over both c_- and c_+ within the graphene nanopore (Fig. S7a and S7c). On the other hand, when $c_0 = 100$ mM, λ_D is much smaller than r_G , and the concentration is only affected by V_G close to the pore edge (Fig. S7b and S7d). Therefore by increasing c_0 (and equivalently reducing λ_D), V_G loses control over the transport in the center of the pore and leads to a lower ξ value. Due to the existence of graphene's quantum capacitance, the surface potential ψ_G is essentially smaller than V_G , and the maximum surface anion concentration ($c_0 = 100$ mM, $V_G = 1.25$ V) is ~ 3 M, much smaller than the saturated surface adsorption density (at the order of 10^2 M^{S8}). Therefore we expect the surface enhancement of the anions under the FEM conditions to be realistic and the influence of the anion concentration on the diffusivity is minimal.^{S9}

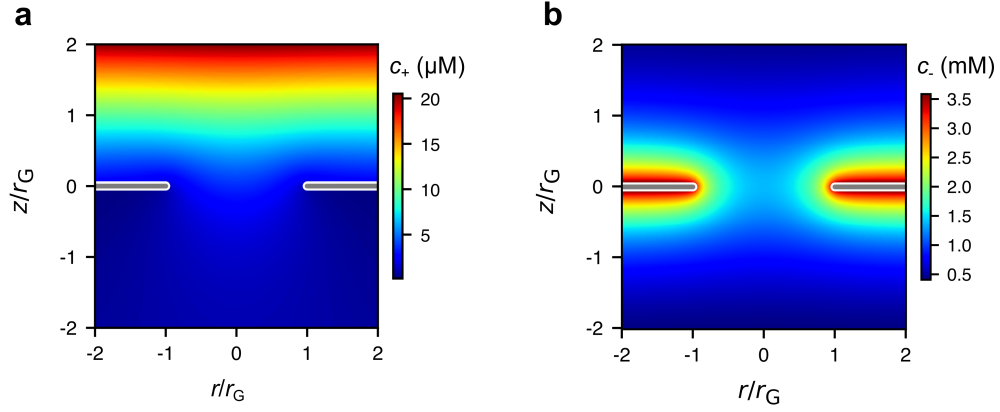


Figure S6: Cation concentration c_+ (a.) and anion concentration c_- (b.) near the graphene nanopore with $r_G = 10$ nm, $c_0 = 0.1$ mM, and $V_G = 0.75$ V, for a KCl solution at 0.1 mM. Depletion of cation and accumulation of anion can be observed near the graphene surface.

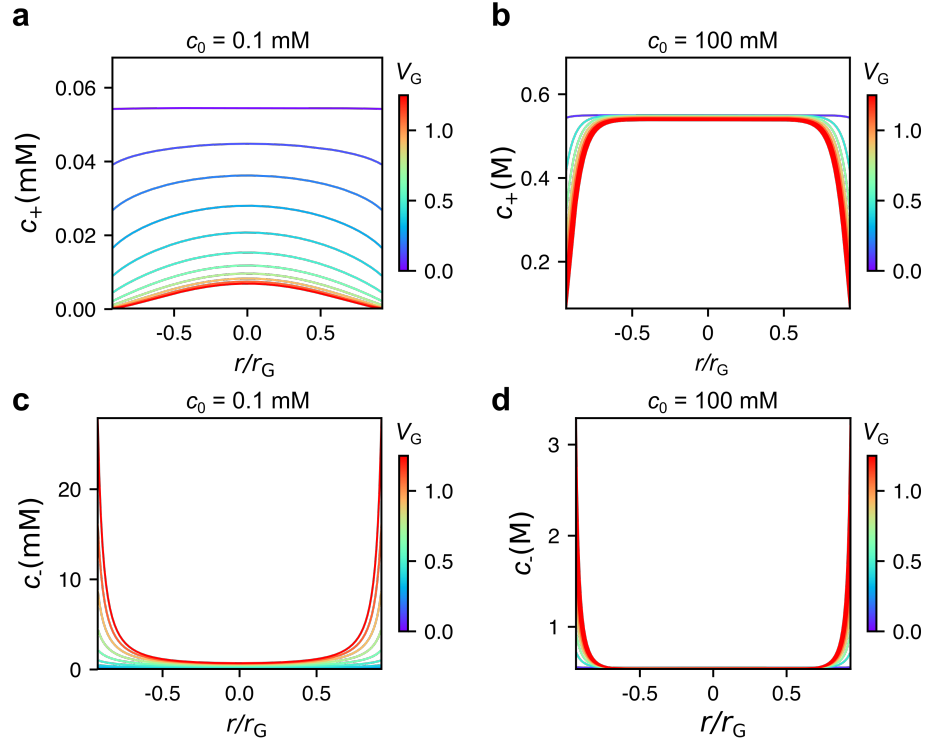


Figure S7: Radial distribution of ions along the line $z = 0$ within a graphene nanopore with $r_G = 10$ nm: (a.) c_+ at $c_0 = 0.1$ mM, (b.) c_+ at $c_0 = 100$ mM, (c.) c_- at $c_0 = 0.1$ mM and (d.) c_- at $c_0 = 100$ mM. The lines with varied colors indicate the difference of V_G applied.

Next we analyze the diffusion and drift contributions to the ionic transport. As shown in Fig. S8, the electrochemical potential energy μ_i is decomposed into the electric potential energy $z_i c_i \psi_i$ (Fig. S8a and S8b) and the chemical potential energy $k_B T \ln x_i$ (Fig. S8c and S8d) near a graphene nanopore with $r_G = 10$ nm and $V_G = 0.75$ V. The transport of cations is dominated by its chemical potential and the diffusion is most pronounced in the center of the pore. The electric and diffusive potentials are similar in magnitude, but with opposite signs, counteracting each other. As a result, different pathways for cations and anions emerge, where cations preferably pass through the pore center, while anions mainly pass near the pore edge, as shown in Fig. S9.

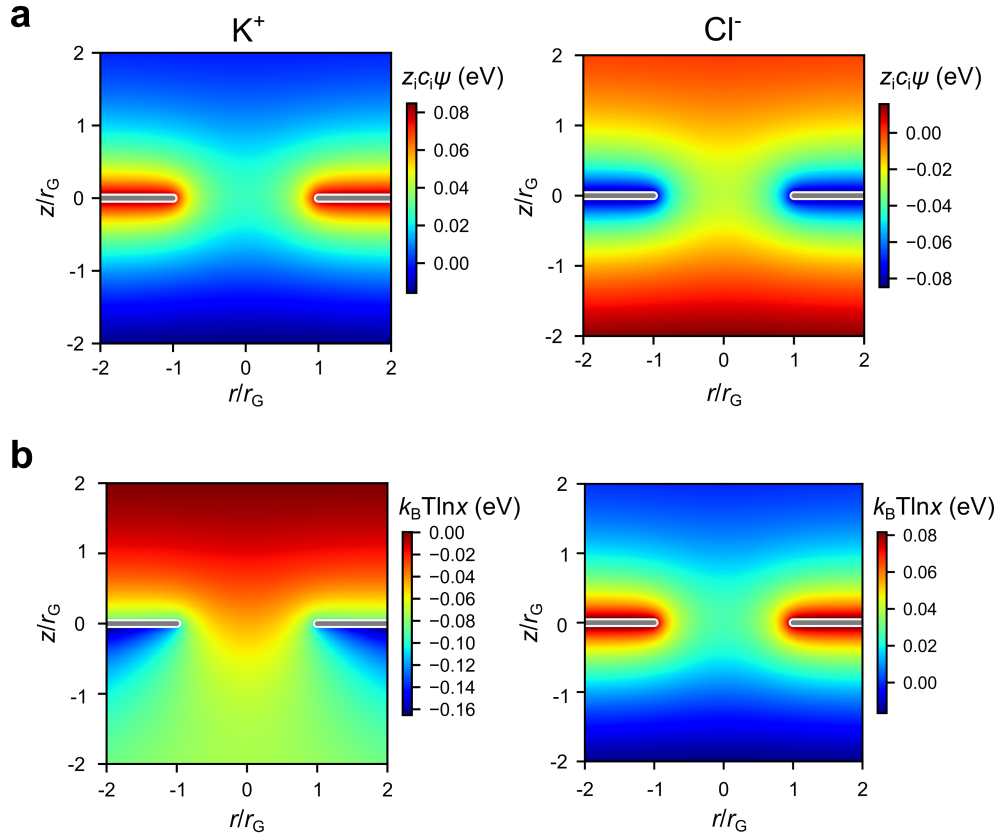


Figure S8: Decomposition of electrochemical potential near a nanopore corresponding to main text Fig.4. **a**. The electrostatic (drift) contribution to the electrochemical potential for cation (left) and anion (right) and **b**. The concentration (diffusion) contribution to the electrochemical potential for cation (left) and anion (right). The relative small order of magnitude for anion electrochemical potential is caused by the balance between the diffusion and drift for anion.

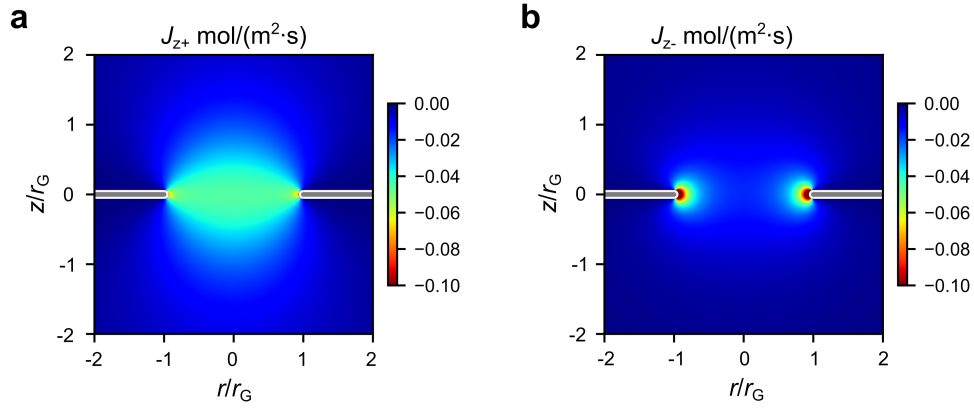


Figure S9: z-component fluxes of cation (J_{z+} , **a.**) and anion (J_{z-} **b.**) near the graphene nanopore corresponding to Fig. 4b in main text. The pathways for the different ions can be spatially distinguished: the flux of cation passes mostly through the center of the graphene nanopore while the anion passes mainly through the edge. The analysis is in consistent with the gradient of chemical potential as shown in the main text Fig. 4b.

We note that when the surface potential ψ_G of graphene further increases, the salt rejection may be weakened, or even enhanced salt transport is observed. To see this, we artificially increase the ψ_G up to over 1 V when not considering the limiting effect of graphene quantum capacitance. As seen in Fig. S10, for each salt concentration c_0 , the averaged total flux J_z does not further decrease when ψ_G is larger than a critical potential V_c . At low c_0 , further increasing ψ_G over V_c may even enhance the flux, leading to a negative ξ . The reserve of the salt rejection at higher V_G values is caused by the enhanced anion flux around the pore edge, while the cation flux saturates (Fig. S11). Such flux enhancement resembles that in an ionic transistor^{S10,S11} when ionic current increases by applying gate voltage. Nevertheless, this regime may not be easily observed experimentally as the V_G applied may already exceed the electrochemical window of water.

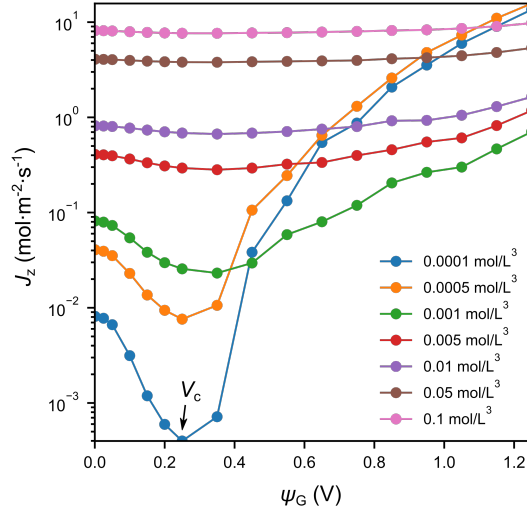


Figure S10: Average total flux J_z in the nanopore as a function of ψ_G at different concentrations. The range of ψ_G is larger than the experimentally achievable value. The rejection of flux becomes weaker after a certain level of ψ_G is reached. Further increasing the surface potential of graphene may even enhance the transportation of ions, which is similar to the cases of ionic transistors.

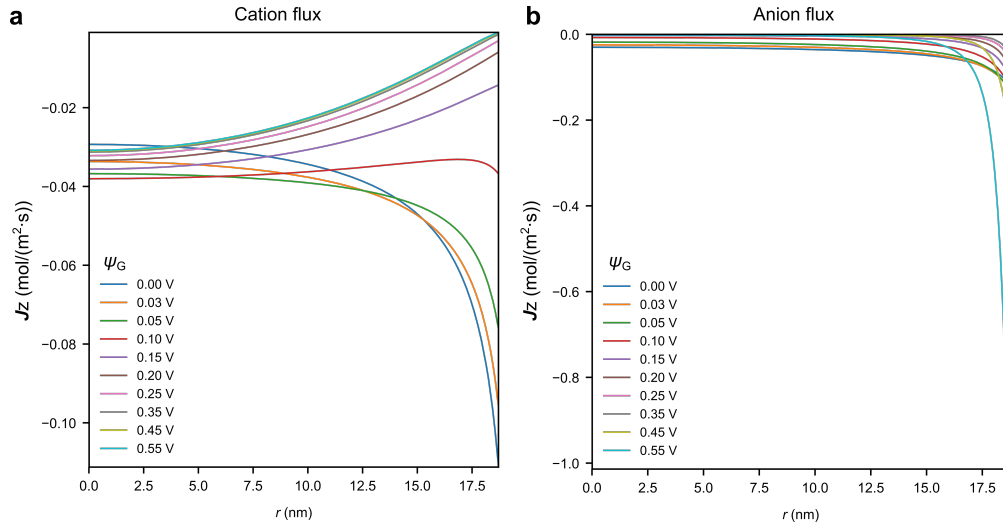


Figure S11: Spatial distribution of J_z at $z = 0$ as a function of r in a nanopore with $r_G = 20$ nm, at different levels of ψ_G (larger than experimentally achievable values) for cation (a.) and anion (b.). The cation flux becomes nearly saturated with increasing ψ_G , while the flow of anion near the pore edge becomes much larger. The drastic increase of pore-bounded anion flux is caused by the accumulation of anions near the graphene surface, and in turn causes the increasing of total flux as seen in Fig.S10.

S8 Effect of pore size distribution

In this section we provide a detailed discussion about the influence of pore size distribution on the salt rejection through the PG-PCTE membrane. Larger pores are the major contributors to salt flux, while at the same time, the effect of rejection is least pronounced. As seen from main text Fig. 1c inset, the average distance between individual nanopores is larger than the largest Debye length studied here (~ 30 nm for 1 mM 1:1 salt solution), we can assume that the ionic transport pathways through different nanopores do not influence each other and the total ionic flux \mathbf{J}_{PG} is the summation of fluxes through individual pores \mathbf{J}_i :

$$\mathbf{J}_{\text{PG}} = \sum_i \mathbf{J}_i = \sum_{r_i} x_{r_i} \mathbf{J}_{r_i} \quad (\text{S8})$$

where r_i is the radius of individual pores, \mathbf{J}_{r_i} and x_{r_i} are the flux of individual pore and the distribution probability when $r_G = r_i$. The salt rejection factor ξ through graphene is then expressed as:

$$\begin{aligned} \xi &= 1 - \frac{\sum_{r_i} \mathbf{J}_{r_i} x_{r_i}}{\sum_{r_i} \mathbf{J}_{r_i} (V_G = 0) x_{r_i}} \\ &= 1 - \frac{\sum_{r_i} \hat{J}_{r_i} r_i^2 x_{r_i}}{\sum_{r_i} \hat{J}_{r_i}^0 r_i^2 x_{r_i}} \\ &\approx \sum_{r_i} \left(1 - \frac{\hat{J}_{r_i}}{\hat{J}_{r_i}^0} \right) w_{r_i} \\ &= \sum_{r_i} \xi_{r_i} w_{r_i} \end{aligned} \quad (\text{S9})$$

where \hat{J} and \hat{J}^0 are the flux normalized by pore area when $V_G = 0$ and $V_G \neq 0$, respectively, $w_{r_i} = x_{r_i} r_i^2 / \sum_{r_i} x_{r_i} r_i^2$ is the contribution to the salt rejection from individual pore rejection rate ξ_{r_i} . The linear combination between ξ_{r_i} and ξ comes from the assumption that \hat{J}^0 is independent of the pore size from the simple Ficknian diffusion.

To get an insight of the influence of the pore size distribution on the salt rejection, we combine Equation S9 with main text Fig. 5b for the salt rejection of a 1:1 electrolyte to get the pore-distribution-related salt rejection, where the pore distribution is taken from the SEM image of real

samples (for instance main text Fig. 1c inset). Fig. S12a shows the contribution w and ξ as a function of r_G for individual pores when $V_G = 1.25$ V. As can be seen, the majority of pores fall within the regime of $\lambda_D/r_G > 1$, corresponding to $\xi(r_G) > 0.6$. As a result, considering the pore distribution reduces the value of ξ to $\sim 80\%$ to that of a single 20 nm-diameter nanopore (Fig. S12b), which is indeed close to the highest ξ values experimentally observed (for 1mM NaCl system). Such high salt rejection even after considering the pore size distribution, can be explained by the non-linear nature of ξ with r_G and V_G . As seen in main text Fig 5b, for large V_G and λ_D/r_G regions, ξ reaches a “plateau” with its value close to 1. For the fabricated PG samples, most pores are within such region when $V_G = 1.25$ V and $c_0 = 0.1$ mM, which gives a minor change of ξ despite the wide span of pore sizes. In other words, although nanopores as large as 60 nm exist in the system, considerably high salt rejection more than 80% can still be achieved.

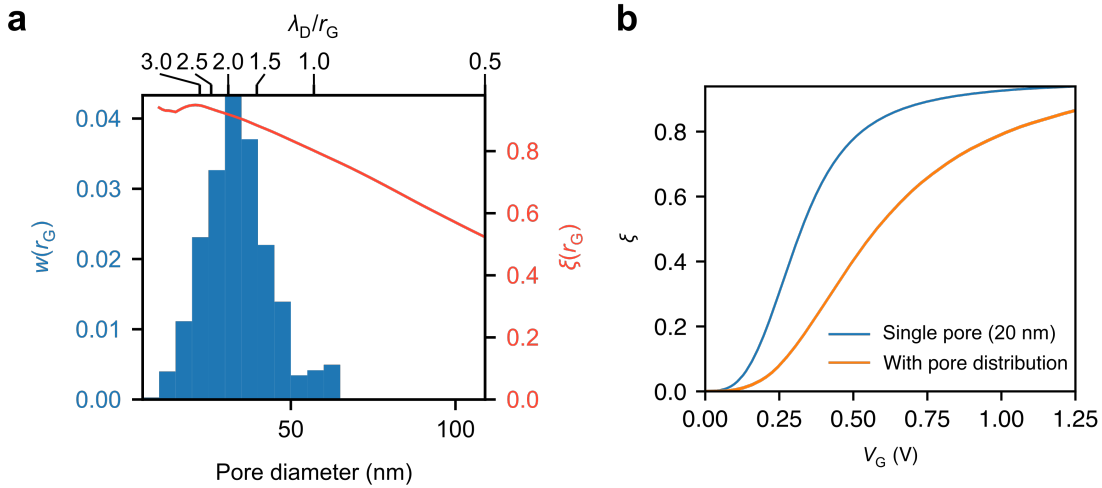


Figure S12: Salt rejection after considering the pore size distribution. **a.** w (left axis) and ξ (right axis) as a function of r_G for the experimental pore size distribution with $c_0 = 0.1$ mM and $V_G = 1.25$ V. **b.** Salt rejection ratio ξ as a function of V_G of a 0.1mM 1:1 salt from a 20 nm-diameter nanopore (blue line) and from the experimental pore size distribution (orange line), by applying Equation S9 to main text Fig. 5b.

To include the pore size distribution effect for all the salts studied, we performed FEM analysis for the salt rejection through single nanopore of different salts with r_G ranges from 2.5 nm to 35 nm, while keeping c_0 constant at 0.1 mM. As shown in Fig. S13, the behavior of ξ vary with the type of salt. As expected, the overall ξ for monovalent salts (KCl, NaCl, LiCl) is larger than

multivalent salts due to the longer Debye length. Moreover, ξ of monovalent salts varies less with the pore size compared with multivalent salts. This can be explained by the non-linear dependency of ξ on λ_D/r_G as discussed above. Combine the FEM-simulated ξ values with the experimental pore size distribution, we obtain main text Fig. 6.

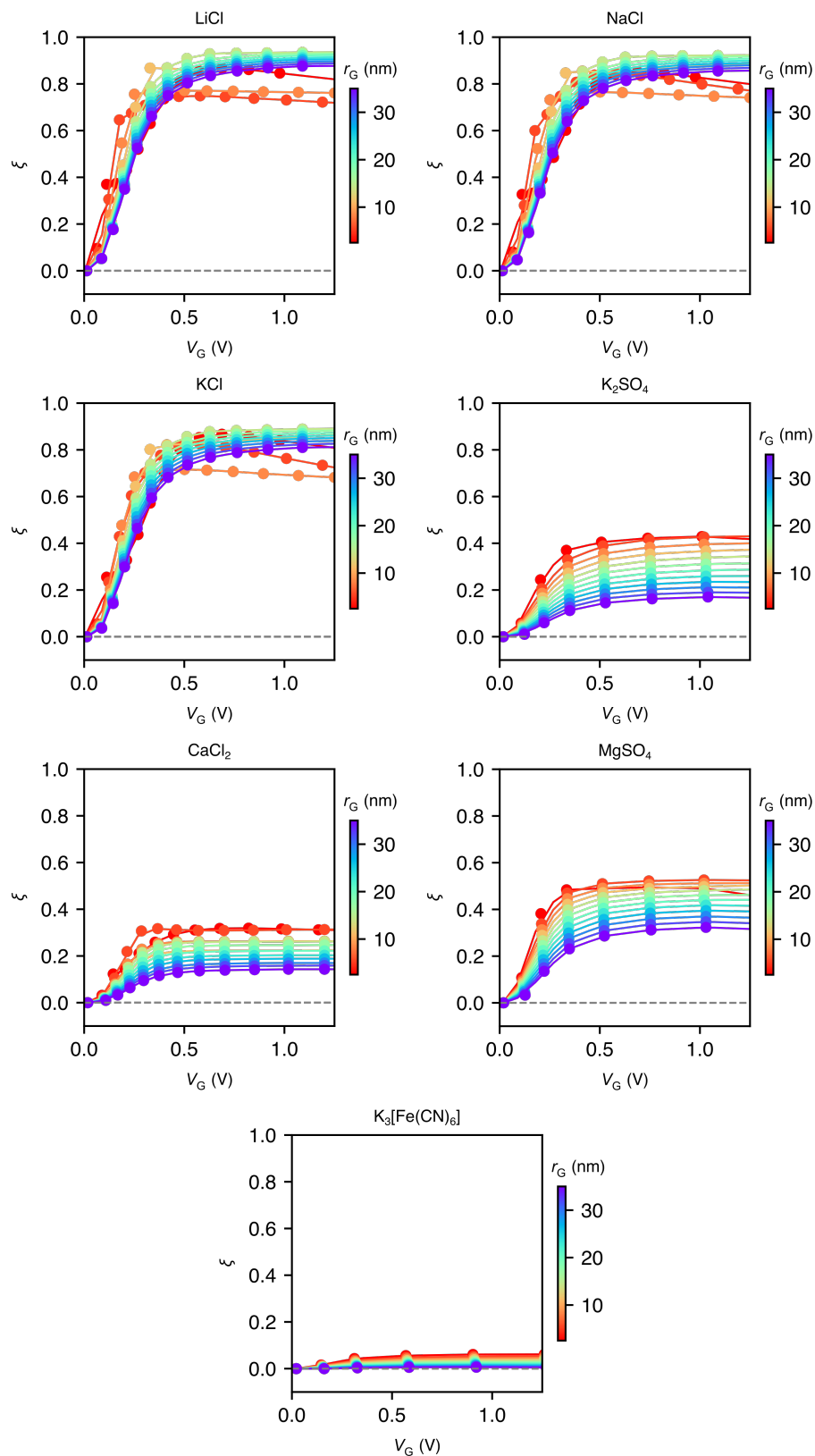


Figure S13: FEM-simulated salt rejection ratio ξ as a function of V_G through single nanopores for different salts with varied pore radius. All salts have concentration $c_0 = 0.1$ mM.

S9 Further details of the numerical simulation

The numerical simulations were carried out using COMSOL Multiphysics 5.3a. The simulation domain is shown in Fig.S14. To simplify the geometry, we use axial symmetric coordinate system. The radius L and height H of both HCR and LCR are set to $20 r_G$, the radius of the nanopore. The potential at the bottom of the LCR and the center of the graphene domains are set to be 0 and ψ_G , respectively. The potential at the end of HCR is not set explicitly, but rather determined through the Poisson equation with no flux boundary condition $\mathbf{D}^{\text{norm}} = 0$. The relative permittivity in the HCR and LCR is set as $\varepsilon = 78$. The relative permittivity of the Stern layer is set to $\varepsilon_H = 20^{S12}$ and for the graphene domain we set the relative permittivity as a large number (e.g. 10^5) for a better convergence of the solver. For the transport of diluted ionic species, we use the PNP equations, to describe the diffusion and drift of the ions, which can be further unified by the gradient of electrochemical potential, as described in the main text. The initial values of the electrolyte is set to c_0 in HCR and $0.1 c_0$ in LCR. At the ends of the cells in the z-direction, we use the inlet boundaries conditions for the concentration of electrolytes, that the concentration on these boundaries remains the same with the initial value, due to the effective mixing in the experimental setup.

The transport of ionic species is described by the steady-state Nernst-Planck equation:

$$\nabla \cdot \mathbf{J}_i = -\nabla \cdot \left(\frac{D_i}{k_B T} c_i N_A \nabla \mu_i \right) = -\nabla \cdot \left(\frac{D_i}{k_B T} c_i N_A [k_B T \nabla \ln x_i + z_i e \nabla \psi] \right) = 0 \quad (\text{S10})$$

$$x_i = \frac{c_i}{\sum_i c_i + c_{\text{H}_2\text{O}}} \quad (\text{S11})$$

The potential distribution within the whole simulation domain is described by the Poisson equation:

$$\nabla \cdot (\varepsilon_m \varepsilon_0 \nabla \psi) = -N_A e \sum_i c_i z_i \quad (\text{S12})$$

Where ε_m is the relative permittivity of domain m. The contribution of mobile charges is only valid in the solution domain. The use of a large ε_G ensures that the potential in the whole simulation domain can be solved continuously.

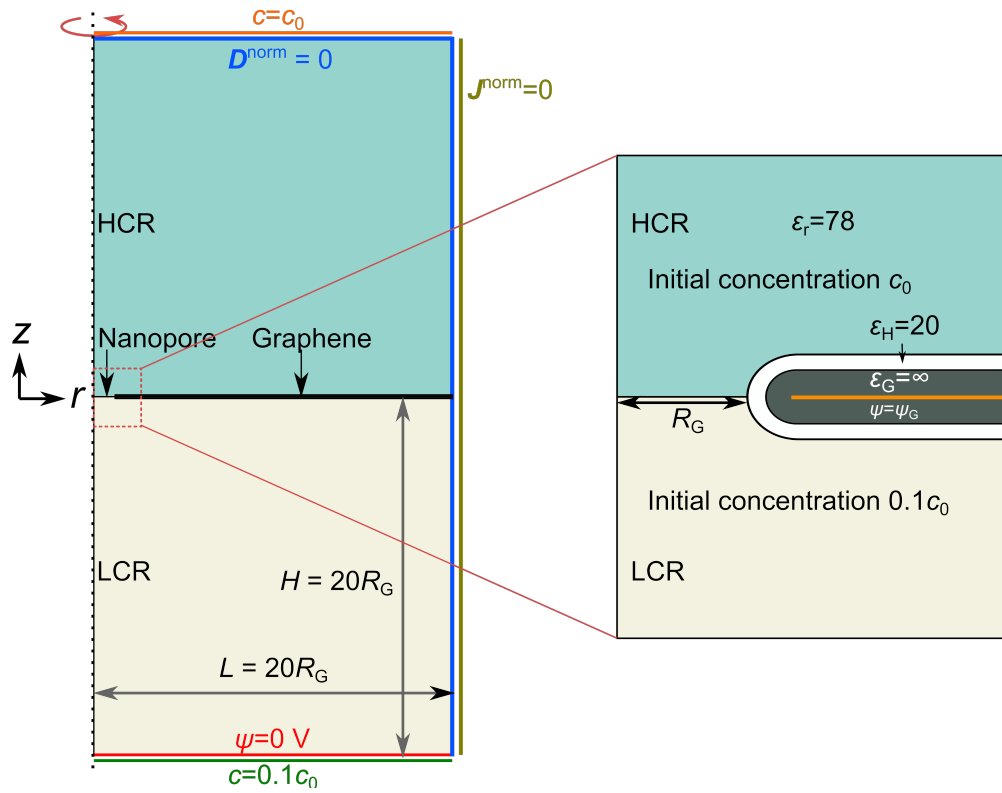


Figure S14: Scheme of the simulation domain used. Left: geometry of the whole simulation domain. Right: configuration near the graphene nanopore, corresponding to the red rectangle on the left side.

To simulate the applied external bias V_G , we set the value of ψ_G explicitly and extract the charge σ_G by:

$$\sigma_G = -\frac{\int_{\Omega} z_i c_i N_A e d^3 \Omega}{S_G} \quad (\text{S13})$$

and V_G is then calculated by:

$$V_G = \Delta\phi_G + \psi_G \quad (\text{S14})$$

$$\sigma_G = \int_0^{\Delta\phi_G} \frac{1}{C_Q(\phi_G)} d\phi_G \quad (\text{S15})$$

where the quantum capacitance $C_Q = \partial\sigma_G/\partial\phi_G$ is calculated by Eq. 8 in main text.

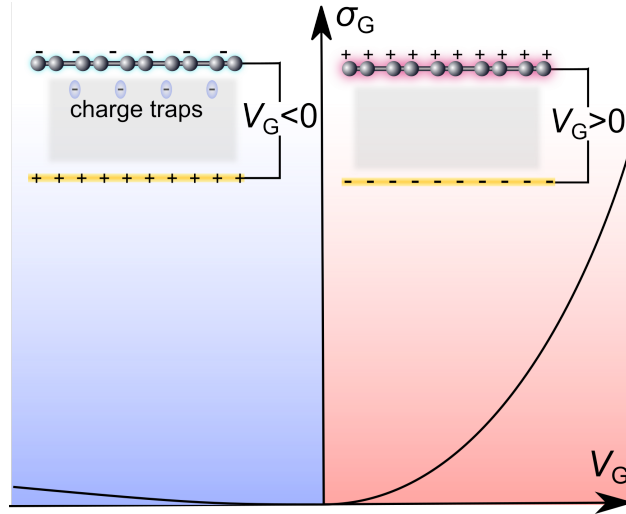


Figure S15: Schematic illustration of the origin of the asymmetric rejection with respect to V_G . Due to the existence of surface charge traps at negative V_G , the graphene is less charged compared to the positive V_G .

Note that due to the existence of electron traps on graphene due to fabrication process, the induced charge traps on graphene effectively reduce the charge density on graphene and greatly attenuate the surface potential on graphene, as illustrated in Fig.S15. This effect is universally observed in CVD-graphene-based field effect transistors in air, while the mechanism is fully understood yet. In view of this, we only simulate the situation where $V_G > 0$ for the salt rejection mechanism. The trend that ξ is almost independent of V_G when $V_G < 0$ can be qualitatively explained by the existence of surface charge traps as stated above. We have also tested the mesh-

independence of our solutions. As shown in Fig. S16a, we use two parameters to control the refinement of the mesh entities: (i) triangle mesh division N_{div} , giving the smallest triangle mesh size δ_G/N_{div} , where δ_G is the thickness of graphene, and (ii) division of mesh N_b , on the boundary $0 < r < r_G; z = 0$. The solution convergence is evaluated by the mean absolute error (MAE) of anion flux \mathbf{J}_z on the boundary $0 < r < r_G; z = 0$, as shown in Fig. S16b. The solution of the PNP model is sensitive to the value N_b , and can be regarded numerically converged when $N_b > 100$. Combining the calculation effort and numerical precision, we adapt the value $N_{\text{div}} = 5$ and $N_b = 100$ in our simulations.

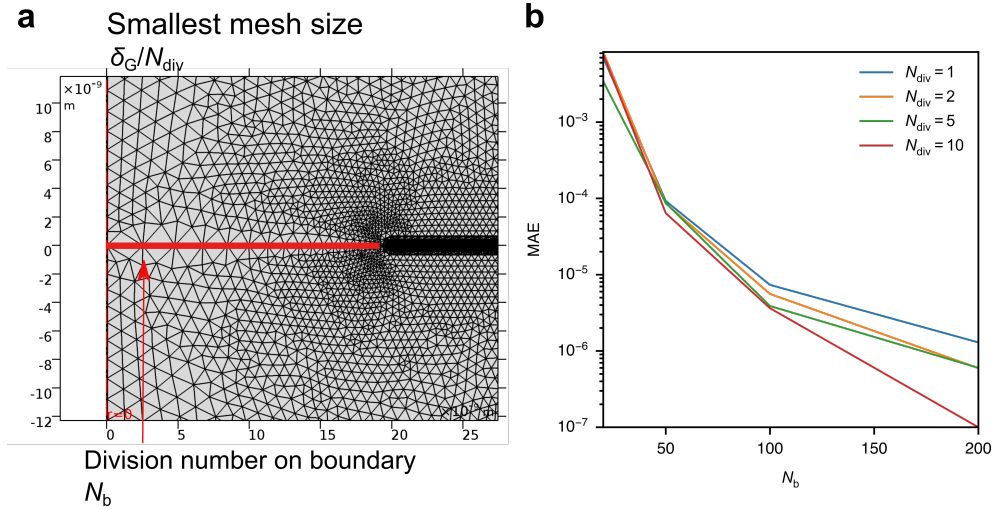


Figure S16: Mesh independence of the solution. **a.** Scheme of the mesh refinement near the graphene pore. The values N_{div} and N_b controls the size of mesh along the boundary $z = 0, 0 < r < r_G$ (shown in red). **b.** Mean absolute error (MAE) of the anion flux \mathbf{J}_z along the boundary $z = 0, 0 < r < r_G$. The error is more sensitive to N_b than N_{div} .

S10 Conductivity and Debye length for all salts

In Table S4, the conductivities and calculated Debye lengths for 6 salts are shown. At the same concentration, the higher ionic strength of the multivalent salts leads to a reduction of the respective Debye lengths.

Table S4: Conductivity and λ_D of various salts.

Solution	Conductivity ($\text{mS}\cdot\text{cm}^{-1}$)	λ_D (nm)
0.1 mM NaCl	1.80×10^{-2}	30.4
0.1 mM LiCl	1.58×10^{-2}	30.4
0.1 mM CaCl_2	2.19×10^{-2}	17.2
0.1 mM MgSO_4	3.27×10^{-2}	15.2
0.1 mM K_2SO_4	4.16×10^{-2}	17.2
0.1 mM $\text{K}_3[\text{Fe}(\text{CN})_6]$	5.95×10^{-2}	12.4

References

- (S1) Choi, K.; Droudian, A.; Wyss, R. M.; Schlichting, K.-P.; Park, H. G. Multifunctional wafer-scale graphene membranes for fast ultrafiltration and high permeation gas separation. *Sci. Adv.* **2018**, *4*, eaau0476.
- (S2) Vanysek, P. Ionic conductivity and diffusion at infinite dilution. *CRC handbook of chemistry and physics* **2000**, 83.
- (S3) O'Hern, S. C.; Boutilier, M. S. H.; Idrobo, J.-C.; Song, Y.; Kong, J.; Laoui, T.; Atieh, M.; Karnik, R. Selective Ionic Transport through Tunable Subnanometer Pores in Single-Layer Graphene Membranes. *Nano Lett.* **2014**, *14*, 1234–1241.
- (S4) Roscoe, R. XXXI. The flow of viscous fluids round plane obstacles. *Philos. Mag.* **1949**, *40*, 338–351.
- (S5) Celebi, K.; Buchheim, J.; Wyss, R. M.; Droudian, A.; Gasser, P.; Shorubalko, I.; Kye, J.-I.; Lee, C.; Park, H. G. Ultimate Permeation Across Atomically Thin Porous Graphene. *Science* **2014**, *344*, 289–292.
- (S6) Hill, T. L. Effect of rotation on the diffusion-controlled rate of ligand-protein association. *Proc. Nat. Acad. Sci.* **1975**, *72*, 4918–4922.

- (S7) Grebenkov, D. S.; Krapf, D. Steady-state reaction rate of diffusion-controlled reactions in sheets. *J. Chem. Phys.* **2018**, *149*, 064117.
- (S8) Bard, A. J.; Faulkner, L. R.; Leddy, J.; Zoski, C. G. *Electrochemical methods: fundamentals and applications*; Wiley New York, 1980; Vol. 2.
- (S9) Tang, L. Concentration dependence of diffusion and migration of chloride ions. *Cement Concrete Res.* **1999**, *29*, 1463–1468.
- (S10) Nam, S.-W.; Rooks, M. J.; Kim, K.-B.; Rossnagel, S. M. Ionic Field Effect Transistors with Sub-10 nm Multiple Nanopores. *Nano Lett.* **2009**, *9*, 2044–2048.
- (S11) Cheng, C.; Jiang, G.; Simon, G. P.; Liu, J. Z.; Li, D. Low-voltage electrostatic modulation of ion diffusion through layered graphene-based nanoporous membranes. *Nat. Nanotechnol.* **2018**, *13*, 685–690.
- (S12) Conway, B. E.; Bockris, J. O.; Ammar, I. A. The dielectric constant of the solution in the diffuse and Helmholtz double layers at a charged interface in aqueous solution. *Trans. Faraday Soc.* **1951**, *47*, 756–766.